

FIG. 1. (Color online). (a) Energy level diagram for the transmon indicating the levels and microwave drives. Inset: optical micrograph of transmon showing Al pads (light grey) on sapphire (dark grey). (b) Cavity transmission at $\omega_{cav}/2\pi = 7.1585$ GHz after the transmon is prepared in state $|0\rangle$ (black line), $|1\rangle$ (blue dash) or $|2\rangle$ (magenta dots). Vertical dashed lines indicate drive powers P_a used in the AT experiment to achieve the readout proportional to $\rho_{11} + \rho_{22}$, and P_b to readout ρ_{22} for ω_{12} calibration. (c) Spectroscopic measurements (black dots) and fit (red line) of ω_{01} . Note small shoulder at 4.292 GHz near the 0-to-1 transition peak at 4.294 GHz. (d) Spectroscopic measurements (black dots) and fit (red line) of ω_{12} .

and lift-off procedures. It has a single Al/AlO_x/Al Josephson junction capacitively shunted by two 375×800 μm Al pads on a sapphire substrate. The tunneling energy of the junction is $E_J/h = 16.5$ GHz, and the pads lower the charging energy to $E_C/h = 177$ MHz. The pads are fabricated as a mesh of 2.5 μm wide lines placed every 10 μm in both directions to enhance expulsion of any external magnetic fields and trap any magnetic vortices already present. The shunting pads also form a dipole antenna which couples the qubit to the cavity with strength $g/2\pi = 151$ MHz. The 3D cavity is a rectangular box made from oxygen-free-high-conductivity Cu, with the fundamental TE₁₀₁ mode at $\omega_{cav}/2\pi = 7.1585$ GHz. This mode is used for qubit readout, with loss limited by the internal quality factor $Q_i = 18,000$. The cavity is probed in transmission, with the output connector coupled much more strongly ($Q_e^{out} = 30,000$) than the input connector ($Q_e^{in} = 120,000$). The cavity is mounted on the mixing chamber of a Leiden Cryogenics CF-450 dilution refrigerator at $T = 22$ mK. The

microwave lines to the cavity are heavily attenuated, filtered and isolated to protect the device from extrinsic noise. The output signal from the cavity is passed to a high-electron-mobility transistor amplifier at the 3 K stage, and then further amplified, mixed down, and digitized at room temperature.²⁶

Three microwave drives are used: cavity, probe, and coupler. The cavity is turned on at time $t = 0$ for 5 μs to record the initial (ground) state of the system, and then again at $t = 290$ μs to read out the final state of the system. Within the 290 μs window between readout pulses, transmon control microwaves (either probe or coupler, or both) are applied. The whole sequence is repeated every 600 μs . The cavity is used solely for the readout, and does not participate in the Autler-Townes manifold.

Measurement of the transmon state is achieved with a high signal-to-noise ratio by using the Jaynes-Cummings non-linearity readout.^{20–22} The cavity pulses are applied at the bare cavity frequency $\omega_{cav}/2\pi = 7.1585$ GHz and with an amplitude that provides maximum contrast between the ground and excited states [Fig. 1(b)]. At amplitude P_a the cavity does not discriminate between the transmon being in $|1\rangle$ or $|2\rangle$, while at P_b it is mostly sensitive to $|2\rangle$. The signal from the non-linearity readout at P_a is proportional to the sum total of the first and second excited state probabilities, ρ_{11} and ρ_{22} , and is used to obtain the 0-to-1 and AT data. The signal at P_b is used for the characterization of 1-to-2 transition only.

We can determine the parameters in Eqs. 1 and 2 from a set of measurements on ω_{01} and ω_{12} as follows. We characterized the ω_{01} transition by applying just the probe and cavity readout tones. By pulsing the probe we find the relaxation time $T_1 = 39$ μs , limited by internal loss. The measured Ramsey decay time $T_2^* = 51$ μs is less than the relaxation-limited value of $2T_1$ due to additional dephasing. This T_2^* can be used to place a bound of less than 0.02 thermal photons in the cavity.³⁰ From T_1 and T_2^* we obtain relaxation (denoted by Γ_{ij} for $|i\rangle \rightarrow |j\rangle$ process) and dephasing (denoted by γ_i for state $|i\rangle$) rates of $\Gamma_{10} = 1/T_1 = 26 \times 10^3$ s^{-1} , $\gamma_2 = \gamma_1 = 1/T_2^* - 1/2T_1 = 6.6 \times 10^3$ s^{-1} . We set $\Gamma_{21} = 1.41 \times 26 \times 10^3$ s^{-1} and $\Gamma_{20} = 0$ based on the ratio of transmon transition matrix elements.²⁷ We assume negligible upward rates in the system, and set $\Gamma_{ij} = 0$ for all $i < j$.

At low probe powers, we observe a small shoulder on the left-hand side of the ω_{01} peak [see Fig. 1(c)], which we attribute to a fluctuator affecting the transmon. Similar fluctuators, possibly due to a microscopic defect in or near the junction, have been studied in other superconducting qubits.^{31–33} Apart from the slight background, the fluctuator does not affect the system in any way. We fit the data using the steady-state solution to Eq. 2, with an additional Lorentzian to account for the fluctuator background [Fig. 1(c)]. With decoherence rates determined independently, we extract best fit values $\Omega_p/2\pi = 186$ kHz, $\omega_{01}/2\pi = 4.294085$ GHz, and the position, width and amplitude of the Lorentzian background.

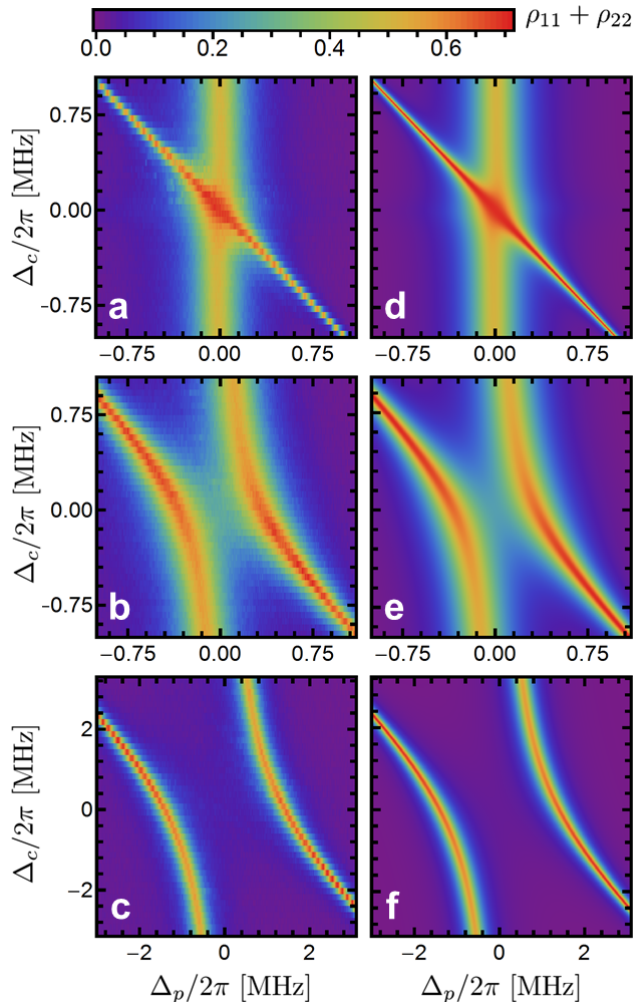


FIG. 2. (Color). (a-c) data and (d-f) simulations of the Autler-Townes splitting for several coupler powers. Coupler strengths are: (a) and (d) 0.177 MHz, (b) and (e) 0.707 MHz, (c) and (f) 2.82 MHz. To account for larger peak separation, the scale is increased on the bottom row of plots.

In order to characterize the ω_{12} transition, we perform a π -pulse at ω_{01} with the probe tone, followed by a π -pulse near ω_{12} with the coupler. We measure the population of $|2\rangle$ alone at a cavity power $P_b \approx P_a - 10$ dB that provides contrast only when $|2\rangle$ is excited [Fig. 1(b)]. The spectroscopic peak [Fig. 1(d)] is fit to obtain $\omega_{12}/2\pi = 4.116\,609$ GHz. To calibrate Ω_c for the AT experiment, the Rabi frequency of the $|1\rangle \leftrightarrow |2\rangle$ transition as a function of coupler amplitude is measured by replacing the π -pulse on the coupler with a variable-length pulse at $\Delta_c = 0$.

Finally, we calibrate the probability scale by performing Rabi oscillations on ω_{01} . We fit the data, and set the amplitude of the fit exponentially decaying sine function to unity. This calibrates ρ_{11} , and, with the readout at cavity power P_a being equally sensitive to ρ_{11} and ρ_{22} , also calibrates $\rho_{11} + \rho_{22}$.

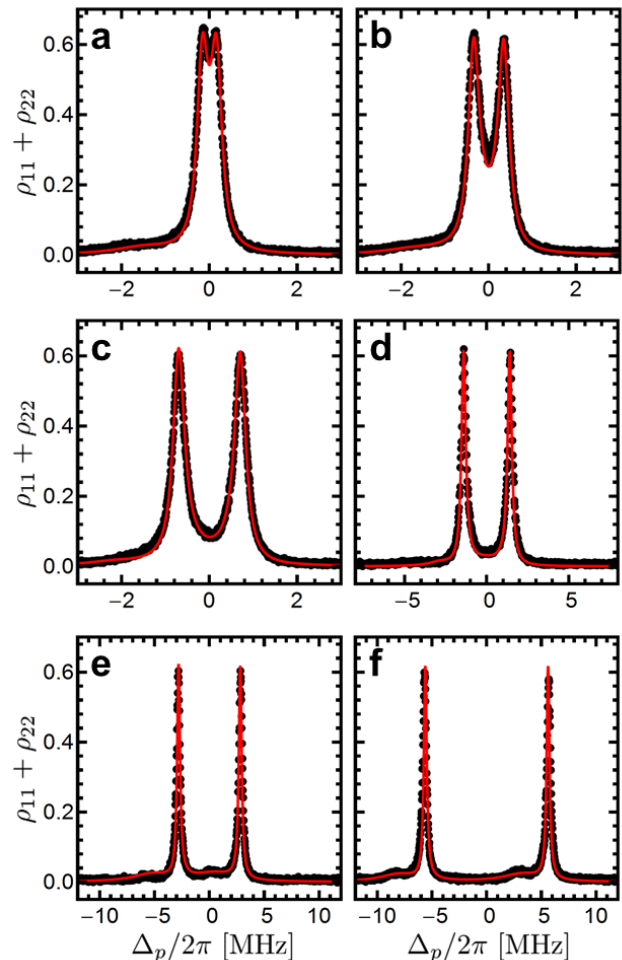


FIG. 3. (Color online). Data (black dots) and simulation (red line) of the Autler-Townes doublet at $\Delta_c = 0$. Coupler strengths are: (a) 0.354 MHz, (b) 0.707 MHz, (c) 1.41 MHz, (d) 2.82 MHz, (e) 5.63 MHz, (f) 11.2 MHz.

For the Autler-Townes experiment, the probe and the coupler are turned on for $280\ \mu\text{s}$ between the two cavity readout pulses. Being much longer than any coherence times in the system, this probe and coupler pulse length ensures the system has achieved a steady state before the measurement. Sweeping both Δ_p and Δ_c around zero, and measuring $\rho_{11} + \rho_{22}$, we observe emergence of the Autler-Townes doublet as Ω_c is increased [see Fig. 2]. At the relatively low coupling drive of $\Omega_c/2\pi = 0.177$ MHz [Fig. 2(a)] we see a crossing of ω_{01} (vertical band) with the two-photon sideband excitation of ω_{02} (diagonal streak). As the coupler strength is increased four-fold, ω_{01} becomes dressed by the coupler photons and shows the emergence of an anti-crossing at zero detuning [Fig. 2(b)]. Increasing Ω_c another four-fold results in a completely separated splitting [Fig. 2(c)]. Figures 2(d-e) show the corresponding simulations found by solving Eq. 2 with no fitting parameters. We find excellent agreement with the data.

To observe a well-separated AT doublet, we must apply sufficiently strong coupler tone while keeping excitations to a three-level manifold. The anharmonicity of the device, $\alpha \equiv \omega_{01} - \omega_{12} = E_C/\hbar = 2\pi \times 177$ MHz, sets an upper limit for the strengths of the drives that can be used. The proximity of the $|0\rangle \leftrightarrow |2\rangle$ two-photon transition at $\omega_{02}/2 = \omega_{01} - \alpha/2$ can also, at sufficiently strong drives, interfere with AT signal.¹⁶ Although the transitions are power-broadened to $\Gamma/2\pi \approx 350$ kHz at this probe amplitude, they remain much smaller than α . Therefore, we require $\Omega_c \gg \Gamma$, $\Omega_c \gg \Omega_p$ for a well-separated AT doublet, as well as the $\Omega_c \ll \alpha$ to restrict the Hilbert space to the three lowest levels.

For coupler detuning $\Delta_c = 0$, the splitting is symmetric around probe detuning $\Delta_p = 0$. As Fig. 3 shows, we see excellent agreement between the data and the density matrix simulation with all parameters independently determined, and an additional Lorentzian added at $\pm\Omega_c/2$ to account for the small background due to the aforementioned fluctuator.

At $\Delta_c = \Delta_p = 0$, the eigenstates of the system can be written in a simple form:²⁵

$$|D\rangle = \cos \Theta |0\rangle - \sin \Theta |2\rangle \quad (3)$$

$$|+\rangle = \frac{1}{\sqrt{2}}[\sin \Theta |0\rangle + |1\rangle + \cos \Theta |2\rangle] \quad (4)$$

$$|-\rangle = \frac{1}{\sqrt{2}}[\sin \Theta |0\rangle - |1\rangle + \cos \Theta |2\rangle] \quad (5)$$

where the mixing angle $\Theta = \tan^{-1}(\Omega_p/\Omega_c)$. State $|D\rangle$ is a dark state with eigenvalue of zero, while states $|\pm\rangle$ correspond to eigenvalues $\pm\sqrt{\Omega_p^2 + \Omega_c^2}$, i.e. separated from the dark state by the generalized Rabi frequency. For large peak separation, the dark state mostly consists of the ground state. In the AT regime the dark state is not achieved by population inversion into $|2\rangle$ but, rather, by having most of the population in $|0\rangle$. Nevertheless, the AT dark state can still be used as the OFF state in router applications due to vanishing contributions of $|1\rangle$ at large peak separations. The fidelity of the dark state can be defined by²⁵

$$\begin{aligned} \mathcal{F}_{|D\rangle} &= \sqrt{\langle D|\rho|D\rangle} \\ &= \frac{\cos 2\Theta}{2}(\rho_{00} - \rho_{22}) - \frac{\sin 2\Theta}{2}(\rho_{20} + \rho_{02}) \\ &\quad + \frac{1}{2}(1 - \rho_{11}). \end{aligned} \quad (6)$$

From the experimental values of Ω_p and Ω_c , as well as the density matrix elements calculated in the simulations, we can infer dark state fidelities of the observed data (Fig. 4). At the two highest coupler powers [$\Omega_c/2\pi = 5.63$ and 11.2 MHz, Figs. 3(e) and 3(f)] the data starts displaying discrepancies from the simulation due to increased proximity to the $\omega_{02}/2$ transition. This is manifested as the AT doublet being pushed to a higher frequency and not centered at $\Delta_p = 0$. The fluctuator

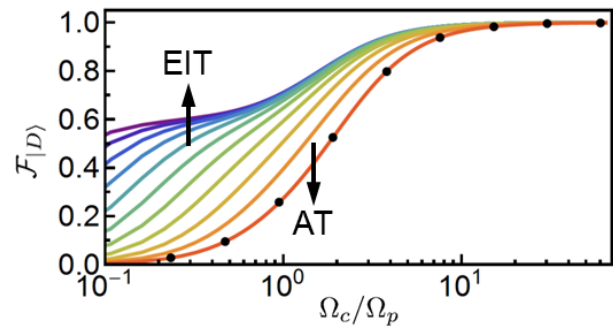


FIG. 4. (Color online). Dark state fidelity inferred from simulations versus coupler power (black dots), and theoretical fidelity (colored lines) for a system with $\Gamma'_{21} = \Gamma_{21}/2^n$, $n = 0, 1, \dots, 9$ (red to violet). A crossover to $\Gamma_{21} \ll \Gamma_{10}$ regime where EIT is possible manifests in the increased fidelity even at small Ω_c/Ω_p .

parameters also change slightly. To account for these discrepancies in our calculation of $\mathcal{F}_{|D\rangle}$, we fit both the AT peaks and the background with Lorentzians to determine new probe detuning, Δ'_p , and new background parameters to feed into the simulation. At the maximum separation (29 linewidths), we calculate the dark state fidelity to be 99.6 – 99.9%. We note that even at the largest coupler powers used, the effects of the higher levels are dispersive, manifesting themselves not as additional excitations but as slight frequency shifts of the doublet.

Figure 4 also shows a theoretical prediction for the scaling of fidelity with Ω_c/Ω_p if our system were in the EIT regime, which would require $\Gamma_{21} \ll \Gamma_{10}$. We model the EIT regime by replacing Γ_{21} by $\Gamma'_{21} = \Gamma_{21}/2^n$ for $n = 0, 1, \dots, 9$ while keeping all other simulation parameters the same. A long-lived $|2\rangle$ makes population trapping in that state possible, opening a narrow EIT window, and resulting in high fidelities even for $\Omega_c/\Omega_p \ll 1$. We believe that the EIT regime can be achieved by engineering the rates of this system.

In summary, we have observed emergence of Autler-Townes splitting in a 3D transmon system by dressing the three lowest levels of the transmon with two drives and reading out the state of the system by pulsing an additional cavity tone. We achieve 99.6 – 99.9% maximum dark state fidelity at 29 linewidths of separation. Even at the highest coupler powers, the data stands in good agreement with a three-level density matrix simulation. Although we do not have a direct measurement of the dark state fidelity, our technique for determining $\mathcal{F}_{|D\rangle}$ as a function of Ω_c/Ω_p using independently measured parameters provides a useful metric for assessing EIT, distinguishing EIT from the Autler-Townes effect, characterizing the ON/OFF ratio, and assessing dark state coherence.

F.C.W. would like to acknowledge support from the Joint Quantum Institute and the State of Maryland

through the Center for Nanophysics and Advanced Ma-

terials. The authors would like to acknowledge Paul Lett and Eite Tiesinga for their helpful discussions.

-
- * snovikov@umd.edu
- ¹ S. Autler and C. Townes, *Phys. Rev.* **100**, 703 (1955).
 - ² C. Cohen-Tannoudji, J. Dupont-Roc, and G. Grynberg, *Atom-Photon Interactions* (Wiley-VCH Verlag GmbH, Weinheim, Germany, 1998).
 - ³ J. Li, G. S. Paraoanu, K. Cicak, F. Altomare, J. I. Park, R. W. Simmonds, M. A. Sillanpää, and P. J. Hakonen, *Sci. Rep.* **2**, 645 (2012).
 - ⁴ I.-C. Hoi, C. M. Wilson, G. Johansson, J. Lindkvist, B. Peropadre, T. Palomaki, and P. Delsing, *New J. Phys.* **15**, 025011 (2013).
 - ⁵ K.-J. Boller, A. Imamoglu, and S. E. Harris, *Phys. Rev. Lett.* **66**, 2593 (1991).
 - ⁶ A. V. Turukhin, V. S. Sudarshanam, M. S. Shahriar, J. A. Musser, B. S. Ham, and P. R. Hemmer, *Phys. Rev. Lett.* **88**, 023602 (2001).
 - ⁷ J. E. Field, K. H. Hahn, and S. E. Harris, *Phys. Rev. Lett.* **67**, 3062 (1991).
 - ⁸ P. M. Anisimov, J. P. Dowling, and B. C. Sanders, *Phys. Rev. Lett.* **107**, 163604 (2011).
 - ⁹ K. V. R. Murali, Z. Dutton, W. D. Oliver, D. S. Crankshaw, and T. P. Orlando, *Phys. Rev. Lett.* **93**, 087003 (2004).
 - ¹⁰ J. L. Picque and J. Pinard, *J. Phys. B* **9**, L77 (1976).
 - ¹¹ P. Cahuzac and R. Vetter, *Phys. Rev. A* **14**, 270 (1976).
 - ¹² C. Delsart and J. C. Keller, *J. Phys. B* **9**, 2769 (1976).
 - ¹³ P. Tamarat, B. Lounis, J. Bernard, M. Orrit, S. Kummer, R. Kettner, S. Mais, and T. Basché, *Phys. Rev. Lett.* **75**, 1514 (1995).
 - ¹⁴ X. Xu, B. Sun, P. R. Berman, D. G. Steel, A. S. Bracker, D. Gammon, and L. J. Sham, *Science* **317**, 929 (2007).
 - ¹⁵ M. Baur, S. Filipp, R. Bianchetti, J. M. Fink, M. Göppl, L. Steffen, P. J. Leek, A. Blais, and A. Wallraff, *Phys. Rev. Lett.* **102**, 243602 (2009).
 - ¹⁶ M. A. Sillanpää, J. Li, K. Cicak, F. Altomare, J. I. Park, R. W. Simmonds, G. S. Paraoanu, and P. J. Hakonen, *Phys. Rev. Lett.* **103**, 193601 (2009).
 - ¹⁷ W. R. Kelly, Z. Dutton, J. Schlafer, B. Mookerji, T. A. Ohki, J. S. Kline, and D. P. Pappas, *Phys. Rev. Lett.* **104**, 163601 (2010).
 - ¹⁸ A. A. Abdumalikov, O. Astafiev, A. M. Zagoskin, Y. A. Pashkin, Y. Nakamura, and J. S. Tsai, *Phys. Rev. Lett.* **104**, 193601 (2010).
 - ¹⁹ H. Paik, D. I. Schuster, L. S. Bishop, G. Kirchmair, G. Catelani, A. P. Sears, B. R. Johnson, M. J. Reagor, L. Frunzio, L. I. Glazman, S. M. Girvin, M. H. Devoret, and R. J. Schoelkopf, *Phys. Rev. Lett.* **107**, 240501 (2011).
 - ²⁰ M. D. Reed, L. DiCarlo, B. R. Johnson, L. Sun, D. I. Schuster, L. Frunzio, and R. J. Schoelkopf, *Phys. Rev. Lett.* **105**, 173601 (2010).
 - ²¹ L. S. Bishop, E. Ginossar, and S. M. Girvin, *Phys. Rev. Lett.* **105**, 100505 (2010).
 - ²² M. Boissonneault, J. M. Gambetta, and A. Blais, *Phys. Rev. Lett.* **105**, 100504 (2010).
 - ²³ A. Kossakowski, *Rep. Math. Phys.* **3**, 247 (1972).
 - ²⁴ G. Lindblad, *Commun. Math. Phys.* **48**, 119 (1976).
 - ²⁵ J. Li, G. S. Paraoanu, K. Cicak, F. Altomare, J. I. Park, R. W. Simmonds, M. A. Sillanpää, and P. J. Hakonen, *Phys. Rev. B* **84**, 104527 (2011).
 - ²⁶ Further details can be found in the Supplemental Material.
 - ²⁷ J. Koch, T. M. Yu, J. Gambetta, A. A. Houck, D. I. Schuster, J. Majer, A. Blais, M. H. Devoret, S. M. Girvin, and R. J. Schoelkopf, *Phys. Rev. A* **76**, 042319 (2007).
 - ²⁸ C. Rigetti, J. M. Gambetta, S. Poletto, B. L. T. Plourde, J. M. Chow, A. D. Córcoles, J. A. Smolin, S. T. Merkel, J. R. Rozen, G. A. Keefe, M. B. Rothwell, M. B. Ketchen, and M. Steffen, *Phys. Rev. B* **86**, 100506(R) (2012).
 - ²⁹ G. J. Dolan, *Appl. Phys. Lett.* **31**, 337 (1977).
 - ³⁰ A. P. Sears, A. Petrenko, G. Catelani, L. Sun, H. Paik, G. Kirchmair, L. Frunzio, L. I. Glazman, S. M. Girvin, and R. J. Schoelkopf, *Phys. Rev. B* **86**, 180504 (2012).
 - ³¹ J. M. Martinis, K. B. Cooper, R. McDermott, M. Steffen, M. Ansmann, K. D. Osborn, K. Cicak, S. Oh, D. P. Pappas, R. W. Simmonds, and C. C. Yu, *Phys. Rev. Lett.* **95**, 210503 (2005).
 - ³² M. Constantin and C. C. Yu, *Phys. Rev. Lett.* **99**, 207001 (2007).
 - ³³ V. Zaretsky, B. Suri, S. Novikov, F. C. Wellstood, and B. S. Palmer, *Phys. Rev. B* **87**, 174522 (2013).